

TOWARDS BEAM HARDENING CORRECTION FOR POLYCHROMATIC X-RAY CT*

Hyoung Suk Park

Department of Computational Science and Engineering, Yonsei University, Seoul, South Korea

Email: jiro7733@yonsei.ac.kr

Hao Gao

*School of Biomedical Engineering and Department of Mathematics, Shanghai Jiao Tong University,
Shanghai, China*

Email: hao.gao.2012@gmail.com

Sung Min Lee and Jin Keun Seo

Department of Computational Science and Engineering, Yonsei University, Seoul, South Korea

Email: sungminlee@yonsei.ac.kr seoj@yonsei.ac.kr

Abstract

High-attenuation object-induced streaking and shadow artifacts in computerized tomography (CT) are somewhat connected to the misfit of the X-ray projection data to the range space of the Radon transform. This misfit is mainly due to the beam hardening factor of the projection data which is unavoidable for polychromatic sources. The major difficulty in dealing with the beam hardening-induced streaking and shadow artifacts comes from its highly nonlinear nature depending on geometries of high attenuation objects. In this work, we investigate the mathematical characteristics of those streaking and shadow artifacts from the structure of the projection data. We also proposed a metal artifacts reduction method by incorporating the recent technique of the nonlinear beam-hardening corrector. Numerical simulations show that the proposed method effectively alleviates the streaking artifacts without changing the background images.

Mathematics subject classification: 65N38, 65N30.

Key words: Computed tomography, Metal artifact reduction, Beam hardening, Radon transform.

1. Introduction

Recently, a significant portion of patients taking CT scans contains high-attenuation objects, due to the rapidly increased number of implanted prostheses associated with a rapidly aging population. Since high-attenuation objects in CT scan may induce serious streaking and shadow artifacts, resulting in loss of information on the region adjacent to high-attenuation objects, there have been a great demand for effective metal artifact reduction (MAR) without affecting important features in CT images. High-attenuation objects causing serious streaking and shadow artifacts include hip replacements, dental fillings, surgical clips, and pacemaker.

The most commonly used CT reconstruction algorithm is the filtered back-projection (FBP) algorithm [6], which is based on the assumption that the projection data is contained in the range space of the Radon transform. However, in the presence of metallic objects, the projection data may not be located near the range space of the Radon transform as shown in Fig. 2.1. It

* Received January 29, 2016 / Revised version received June 2, 2016 / Accepted July 11, 2016 /
Published online December 16, 2016 /

seems that the degree of the discrepancy is somewhat connected to the streaking and shadow artifacts in CT images reconstructed by least square-based schemes, which seek to minimize the difference between the projection data and the Radon transform of an image function.

Over the past few decades, numerous researches on MAR have been conducted to deal with these metallic object-induced streaking and shadow artifacts. The dual-energy CT (DECT) [2] can provide the virtual monochromatic CT image (which are less affected by the metal artifacts due to beam hardening effects) using two non-linear projection data generated at two different energies. However, DECT requires a additional dose of radiation compared with single-energy CT [8]. Most of existing MAR methods can be classified into statistical iterative reconstruction methods [9,10,18,22,32], data completion/inpainting-based methods [1,4,13,15,19,23,28], and hybrid methods combining the aforementioned methods [16]. However, these existing methods have their own limitations; the iterative reconstruction techniques requires prior knowledge of energy-dependent attenuation coefficients of the materials to be imaged and the incident X-ray spectrum [30], and the use of inpainting methods may introduce new artifacts [19,20]. It would be desirable to develop a novel method of extracting streaking and shadow artifacts without affecting intact anatomical images.

In this paper, we shall limit ourselves on metal streaking and shadow artifacts induced by beam hardening, although there are several other causes of streak artifacts such as scatter, nonlinear partial volume effects, photon starvation, motion, and edge effects [5,19]. The beam hardening is brought from the inherent polychromatic nature of medical X-ray source. Metallic object-associated beam hardening causes a severe discrepancy between X-ray projection data and the sinogram space, the range space of the Radon transform. We investigate how the beam hardening-induced discrepancy is linked to the streaking and shadow artifacts. Given a projection data P , let ΠP denote its orthogonal projection onto the sinogram space, as shown in Fig. 2.1. We observed that the degree of the discrepancy $\Pi P - P$ is linked to the streaking and shadow artifacts. From this observation, we conjecture the followings: If $\Pi P - P = 0$, there is no artifacts except cupping artifacts. On the other hand, if the L^2 norm of $\Pi P - P$ is not small, any least square solutions or FBP may not provide acceptable images. A rationale for this observation is provided in Section 2.

In Section 3, we propose a reconstruction method using the recent MAR technique of the geometric corrector invented by Park *et al.* [26], which can handle the inconsistency of projection data P . The geometric corrector is a function of metal geometries and a control parameter associated with all energy-dependent factors including attenuation coefficients and the spectrum of X-ray source. The novelty of the geometric corrector [26] is to extract the metal-induced streaking and shadow artifacts selectively without affecting intact anatomical images when prior knowledge about the shapes of metallic object is available. The proposed method takes advantage of this geometric corrector to compute the parameter and the target image (beam hardening-free image) simultaneously. In addition, to suppress the noise artifacts, total-variation regularization [29] is imposed on a proposed model, and this model is efficiently solved by the augmented Lagrangian method [11,27]. We conducted numerical simulations to evaluate the performance of the proposed method.

2. Method

Let Ω be a cross-sectional slice to be imaged. Let $f(\mathbf{x}, E)$ be the attenuation coefficient at point $\mathbf{x} = (x_1, x_2) \in \Omega$ and energy level E . Throughout this section, we assume that high

density materials occupy the subdomains $D_1, D_2 \dots, D_N$ of Ω . Then, $f(\mathbf{x}, E)$ can be expressed approximately as [14]:

$$f(\mathbf{x}, E) \approx f_0(\mathbf{x}) + \sum_{i=1}^N \mu_{D_i}(E)\chi_{D_i}(\mathbf{x}), \tag{2.1}$$

where μ_D denotes the linear attenuation coefficient of the material occupying the region D . Here, f_0 represents the attenuation coefficient distribution for tissues, which are approximately independent to energy level E .

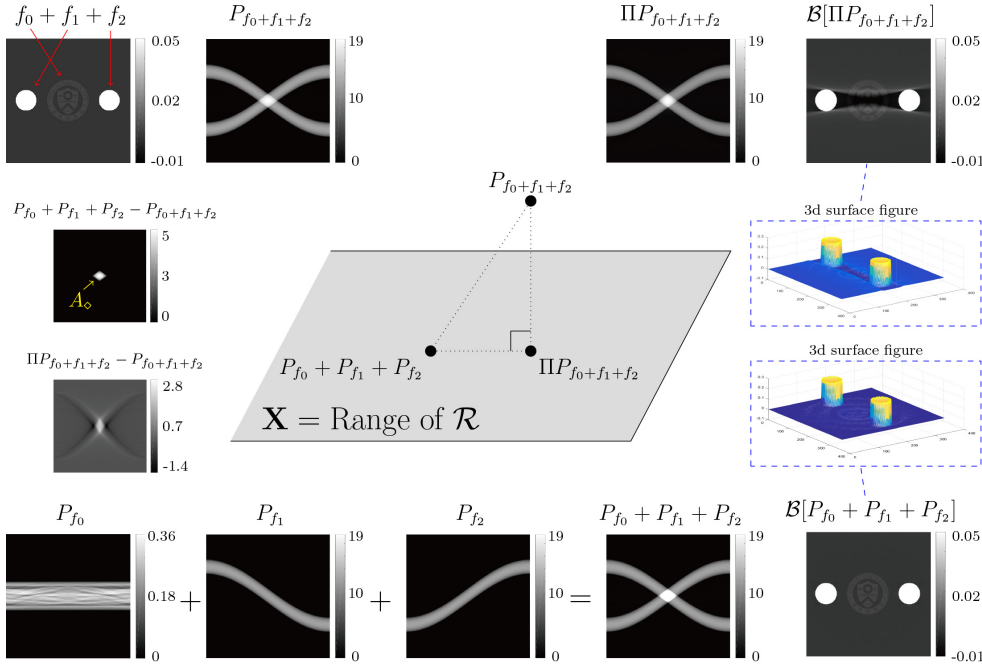


Fig. 2.1. Illustration of the phenomenon in Observation 2.1.

The projection data $P_f(\varphi, s)$ at direction $\boldsymbol{\theta} = (\cos \varphi, \sin \varphi)$, $\varphi \in [0, 2\pi)$, is given by

$$P_f(\varphi, s) = -\ln \left(\int_{\underline{E}}^{\overline{E}} \eta(E) \exp \{ -\mathcal{R}f(\varphi, s, E) \} dE \right), \tag{2.2}$$

where $\eta(E)$ represents a normalized X-ray spectrum with its support in the interval $[\underline{E}, \overline{E}]$, i.e., $\int_{\underline{E}}^{\overline{E}} \eta(E)dE = 1$, and \mathcal{R} is the Radon transform given by

$$\mathcal{R}f(\varphi, s, E) = \int_{\mathbb{R}^2} f(\mathbf{x}, E)\delta(\boldsymbol{\theta} \cdot \mathbf{x} - s) d\mathbf{x}. \tag{2.3}$$

Here, δ is the dirac delta function. It is well known that the linear map \mathcal{R} is bounded from $H^{\alpha-1/2}(\mathbb{R}^2)$ to $H^\alpha([0, 2\pi) \times \mathbb{R})$ [21]. The commonly used CT reconstruction method is the filtered backprojection algorithm (FBP) given by

$$\mathcal{B}[P_f](\mathbf{x}) = \frac{1}{4\pi^2} \int_0^{2\pi} \int_{\mathbb{R}} \frac{\partial}{\partial s} P_f(\varphi, s) \frac{1}{\mathbf{x} \cdot \boldsymbol{\theta} - s} ds d\varphi = \frac{1}{4\pi} \mathcal{R}^* \left(\mathcal{H} \left[\frac{\partial}{\partial s} P_f \right] \right) (\mathbf{x}), \tag{2.4}$$

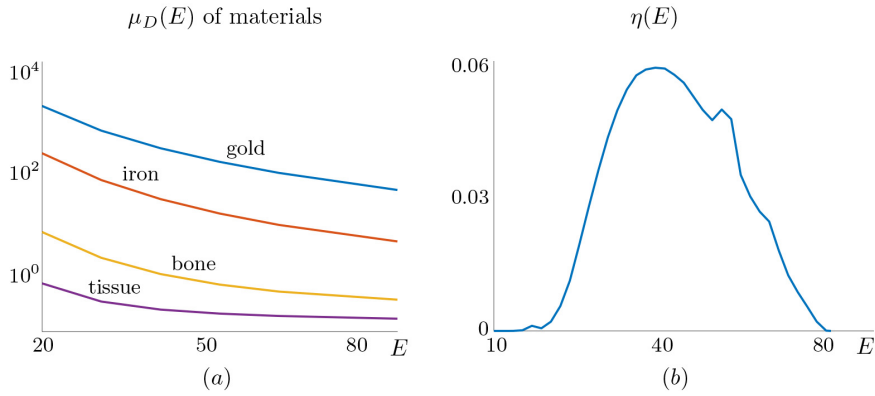


Fig. 2.2. Illustration of linear attenuation coefficient $\mu_D(E)$ of the materials such as iron, gold, bone and tissue in the interval $[20, 80]$ (keV) with a log-scale on y-axis (a), and normalized X-ray spectrum $\eta(E)$ for tungsten anode generated at a tube voltage 80 kVp (b) [7].

where \mathcal{H} is the Hilbert transform with respect to the variable s and \mathcal{R}^* is the backprojection operator (the dual of \mathcal{R}) defined using duality:

$$\int_0^{2\pi} \int_{\mathbb{R}} \mathcal{R}f(\varphi, s)g(\varphi, s)dsd\varphi = \int_{\mathbb{R}^2} f(\mathbf{x}) \underbrace{\left[\int_0^{2\pi} g(\varphi, \mathbf{x} \cdot \boldsymbol{\theta})d\varphi \right]}_{\mathcal{R}^*g(\mathbf{x})} d\mathbf{x}, \tag{2.5}$$

Fig. 2.2 shows the linear attenuation coefficient $\mu_D(E)$ of the materials such as gold, iron, bone and tissue (Fig. 2.2 (a)), and normalized X-ray spectrum $\eta(E)$ (Fig. 2.2 (b)).

Observation 2.1. Let $X \subset L^2([0, 2\pi) \times \mathbb{R})$ be the range space of the Radon transform \mathcal{R} . Let Π be the map from $L^2([0, 2\pi) \times \mathbb{R})$ onto X given by

$$\Pi P = \arg \min_{G \in X} \|P - G\|_{L^2([0, 2\pi) \times \mathbb{R})} \quad \text{for } P \in L^2([0, 2\pi) \times \mathbb{R}). \tag{2.6}$$

We have the followings.

1. For $P_f \in L^2([0, 2\pi) \times \mathbb{R})$,

$$\mathcal{R}\mathcal{B}[P_f] = \Pi P_f \quad \text{and} \quad \mathcal{B}[P_f] = \arg \min_{g \in H^{-1/2}(\mathbb{R}^2)} \|P_f - \mathcal{R}g\|_{L^2([0, 2\pi) \times \mathbb{R})}. \tag{2.7}$$

2. Let D_1 and D_2 , respectively, be two disjoint disks centered at \mathbf{x}_1 and \mathbf{x}_2 with radius being r_1 and r_2 . Let $f_0 \in L^2(\Omega)$ and let $f_i(\mathbf{x}, E) = \mu(E)\chi_{D_i}(\mathbf{x})$ and $i = 1, 2$ with $\mu(E)$ being the linear attenuation coefficient of a high density object at energy level E . Then we have

- (a) $\Pi P_{f_0+f_i} = P_{f_0+f_i}$ and $\mathcal{B}[P_{f_0+f_i}](\mathbf{x}) = f_0(\mathbf{x}) + \rho_i(|\mathbf{x} - \mathbf{x}_i|)\chi_{D_i}(\mathbf{x})$ for $i = 1, 2$, where $\rho_i : [0, r_i] \rightarrow (0, \infty)$ is a monotonically increasing function expressing cupping artifacts in D_i . Hence, $\mathcal{B}[P_{f_0} + P_{f_1} + P_{f_2}]$ does not contain any artifact in $\Omega \setminus D_1 \cup D_2$.
- (b) $\Pi P_{f_0+f_1+f_2} \neq P_{f_0+f_1+f_2}$. The misfit of $\Pi P_{f_0+f_1+f_2} - P_{f_0+f_1+f_2}$ is connected closely to the difference $P_{f_1+f_2} - (P_{f_1} + P_{f_2})$, which generates the streaking and shadow artifacts in CT images.

To give the proof of the above observations, let $\Phi(g) = \|P_f - \mathcal{R}g\|_{L^2([0,2\pi] \times \mathbb{R})}^2$. Then, for all $u \in H^{-1/2}([0, 2\pi) \times \mathbb{R})$ with compact support and $t \in \mathbb{R}$, we have

$$\begin{aligned} \left. \frac{d}{dt} \Phi(g + tu) \right|_{t=0} &= -2 \int_0^{2\pi} \int_{\mathbb{R}} (P_f(\varphi, s) - \mathcal{R}g(\varphi, s)) \mathcal{R}u(\varphi, s) d\varphi ds \\ &= -2 \int_{\mathbb{R}^2} u(\mathbf{x}) \mathcal{R}^* [P_f - \mathcal{R}g](\mathbf{x}) d\mathbf{x}. \end{aligned} \tag{2.8}$$

The last equality follows from the duality of \mathcal{R}^* in (2.5). From (2.8), the direction for which $\Phi(g)$ decreases most rapidly is given by $u = \mathcal{R}^*[P_f - \mathcal{R}g]$, and Φ attains its minimum at g being $0 = \mathcal{R}^*[P_f - \mathcal{R}g]$. Now, we are ready to prove

$$(\mathcal{R}^* \mathcal{R})^{-1} \mathcal{R}^* P_f = \mathcal{B}[P_f]. \tag{2.9}$$

Note that for $f(\mathbf{x})$ and $g(\varphi, s)$, we have [21]

$$\mathcal{R}^* \mathcal{R} f(\mathbf{x}) = \frac{1}{4\pi^2} \int_{\mathbb{R}^2} \int_{\mathbb{R}^2} \frac{4\pi}{|\boldsymbol{\xi}|} f(y) e^{i\boldsymbol{\xi} \cdot (\mathbf{x} - \mathbf{y})} d\mathbf{y} d\boldsymbol{\xi}, \tag{2.10}$$

$$\mathcal{F}_2[\mathcal{R}^* g](\boldsymbol{\xi}) = \frac{2\pi}{|\boldsymbol{\xi}|} \left[\mathcal{F}_1[g](\varphi_{\boldsymbol{\xi}}, |\boldsymbol{\xi}|) + \mathcal{F}_1[g](-\varphi_{\boldsymbol{\xi}}, -|\boldsymbol{\xi}|) \right], \tag{2.11}$$

where $(\cos \varphi_{\boldsymbol{\xi}}, \sin \varphi_{\boldsymbol{\xi}}) = \frac{\boldsymbol{\xi}}{|\boldsymbol{\xi}|}$ and \mathcal{F}_n is the n -dimensional Fourier transform given by

$$\mathcal{F}_n[g](\boldsymbol{\xi}) = \int_{\mathbb{R}^n} g(\mathbf{x}) e^{-i\boldsymbol{\xi} \cdot \mathbf{x}} d\mathbf{x}. \tag{2.12}$$

From (2.10) and (2.11), we have

$$\begin{aligned} (\mathcal{R}^* \mathcal{R})^{-1} \mathcal{R}^* P_f(\mathbf{x}) &= \frac{1}{4\pi^2} \int_{\mathbb{R}^2} \int_{\mathbb{R}^2} \frac{|\boldsymbol{\xi}|}{4\pi} \mathcal{R}^* P_f(\mathbf{y}) e^{i\boldsymbol{\xi} \cdot (\mathbf{x} - \mathbf{y})} d\mathbf{y} d\boldsymbol{\xi} \\ &= \frac{1}{8\pi^2} \int_{\mathbb{R}^2} \left[\mathcal{F}_1[P_f](\varphi_{\boldsymbol{\xi}}, |\boldsymbol{\xi}|) + \mathcal{F}_1[P_f](-\varphi_{\boldsymbol{\xi}}, -|\boldsymbol{\xi}|) \right] e^{i\boldsymbol{\xi} \cdot \mathbf{x}} d\boldsymbol{\xi} \\ &= \frac{1}{16\pi^2} \int_0^{2\pi} \int_{\mathbb{R}} |\omega| \left[\mathcal{F}_1[P_f](\varphi, \omega) + \mathcal{F}_1[P_f](-\varphi, -\omega) \right] e^{i\omega\boldsymbol{\theta} \cdot \mathbf{x}} d\omega d\varphi. \end{aligned} \tag{2.13}$$

The last equality (2.13) follows from $\boldsymbol{\xi} = \omega\boldsymbol{\theta}$.

Using $\mathcal{F}_1[P_f](\varphi, \omega) = \mathcal{F}_1[P_f](-\varphi, -\omega)$ and the fact that $\mathcal{F}_1[\mathcal{H} \frac{\partial}{\partial t} P_f](\varphi, \omega) = |\omega| \mathcal{F}_1[P_f](\varphi, \omega)$ [21], we have

$$\begin{aligned} (\mathcal{R}^* \mathcal{R})^{-1} \mathcal{R}^* P_f(\mathbf{x}) &= \frac{1}{8\pi^2} \int_0^{2\pi} \int_{\mathbb{R}} |\omega| \mathcal{F}_1[P_f](\varphi, \omega) e^{i\omega\boldsymbol{\theta} \cdot \mathbf{x}} d\omega d\varphi \\ &= \frac{1}{4\pi} \int_0^{2\pi} \frac{1}{2\pi} \int_{\mathbb{R}} \mathcal{F}_1 \left[\mathcal{H} \frac{\partial}{\partial s} P_f \right](\varphi, \omega) e^{i\omega\boldsymbol{\theta} \cdot \mathbf{x}} d\omega d\varphi \\ &= \mathcal{B}[P_f]. \end{aligned} \tag{2.14}$$

This completes the proof of the Observation 2.1.1.

Next, we provide a rationale for the second observation which considers the special case where two metallic disks D_1 and D_2 are contained in the field of view of CT. As shown in Fig. 2.1, the data P_f is consistent in all the regions except the diamond shaped area $A_{\diamond} := \{(\varphi, s) : \mathcal{R}\chi_{D_1}(\varphi, s)\mathcal{R}\chi_{D_2}(\varphi, s) \neq 0\}$, that is,

$$P_{f_0+f_1+f_2} = P_{f_0} + P_{f_1} + P_{f_2} \quad \text{in } [0, 2\pi) \times R \setminus A_{\diamond}.$$

On the other hand, P_f is inconsistent only in the small diamond region A_\diamond . From the nature of the orthogonal projection Π onto the sinogram space, this local inconsistency on the diamond region A_\diamond generates the global discrepancy $\Pi P_f - P_f \neq 0$ on the entire region $[0, 2\pi) \times \mathbb{R}$. Since the least square-based CT reconstruction (or FBP) inherently uses the globally corrupted data ΠP_f instead of the locally inconsistent data P_f , the reconstructed image $\mathcal{B}[P_f]$ contains streaking and shadow artifacts.

On the other hand, in the case when the projection data is $P_{f_0+f_1}$ (i.e. the beam-hardening is generated by the single disk D_1), there is no streaking and shadow artifacts. Definitely, as a result of beam-hardening, the reconstructed image $\mathcal{B}[P_{f_0+f_1}]$ contains cupping artifacts inside of the region D_1 , but this cupping artifact does not destroy the intact image outside D_1 . The reason is that $\Pi P_{f_0+f_1}$ is exactly the same as $P_{f_0+f_1}$, that is, no discrepancy ($\Pi P_{f_0+f_1} - P_{f_0+f_1} = 0$) in this case. 3D surface figures of $\mathcal{B}[\Pi P_{f_0+f_1+f_2}]$ and $\mathcal{B}[P_{f_0} + P_{f_1} + P_{f_2}]$ in Fig. 2.1 illustrates these phenomenons.

2.1. Metal artifacts correction algorithm

The goal of MAR is to reveal anatomical and pathological features by reducing high attenuation-induced artifacts. This section suggests a beam hardening correction method using the nonlinear beam-hardening corrector [26]. Let high attenuation objects occupy a two dimensional region $D = \cup_{i=1}^N D_i$ in the CT scan plane. Let $\mu_{D_i}(E)$ be the linear attenuation coefficient of the object D_i at E . For a fixed $E_0 \in [\underline{E}, \overline{E}]$, assume that the linear attenuation coefficients μ_D in (2.1) is approximated by

$$\mu_{D_i}(E) \approx \mu_{D_i}(E_0) + (E - E_0) \left. \frac{\partial \mu_{D_i}}{\partial E} \right|_{E=E_0}. \quad (2.15)$$

Then, the distribution of attenuation coefficient $f(\mathbf{x}, E)$ in (2.1) can be expressed as [24, 25]

$$f(\mathbf{x}, E) \approx f_0(\mathbf{x}) + \sum_{i=1}^N [\mu_{D_i}(E_0) \chi_{D_i}(\mathbf{x})] + (E - E_0) \sum_{i=1}^N \left[\left. \frac{\partial \mu_{D_i}}{\partial E} \right|_{E=E_0} \chi_{D_i}(\mathbf{x}) \right] \quad (2.16)$$

for $(\mathbf{x}, E) \in (\Omega \times [\underline{E}, \overline{E}])$. Our numerical simulation show that (2.16) is a good approximation to reduce the streaking and shadow artifacts in $B[P_f]$. With the assumption (2.16), the projection data P_f in (2.2) can be approximated as

$$P_f(\varphi, s) \approx \mathcal{R}f_0(\varphi, s) + \sum_{i=1}^N \left[\mu_{D_i}(E_0) \mathcal{R}\chi_{D_i}(\varphi, s) \right] - \ln \int_{\underline{E}}^{\overline{E}} \eta(E) \exp \left\{ - (E - E_0) \sum_{i=1}^N \left[\alpha_i \mathcal{R}\chi_{D_i}(\varphi, s) \right] \right\} dE, \quad (2.17)$$

where $\alpha_i = \left. \frac{\partial \mu_{D_i}}{\partial E} \right|_{E=E_0}(\mathbf{x})$ on D_i and 0 otherwise.

We try to eliminate the beam-hardening factors in the projection P_f , in order to reconstruct the target image $f_{\text{target}} = f_0 + \sum_{i=1}^N [\mu_{D_i}(E_0) \chi_{D_i}]$. According to the derivation of the beam-hardening corrector [26], the inconsistency term $P_f - \mathcal{R}f_{\text{target}}$ can be expressed as

$$[P_f - \mathcal{R}f_{\text{target}}](\varphi, s) \approx \psi_{D, \lambda}(\varphi, s), \quad (2.18)$$

where $\boldsymbol{\lambda} = (\lambda_1, \lambda_2, \dots, \lambda_N)$ is an unknown parameter depending on the incident X-ray spectrum $\eta(E)$ and variation of the linear attenuation coefficient $\mu_{D_i}(E)$ with respect to E , and

$$\psi_{D,\boldsymbol{\lambda}}(\varphi, s) = -\ln \left(\frac{\sinh \left(\sum_{i=1}^N \lambda_i \mathcal{R} \chi_{D_i}(\varphi, s) \right)}{\sum_{i=1}^N \lambda_i \mathcal{R} \chi_{D_i}(\varphi, s)} \right). \quad (2.19)$$

Based on the above approximation (2.18), we propose the following minimization problem for determining both the unknown target image f and the parameter $\boldsymbol{\lambda} \in \mathbb{R}^N$:

$$\arg \min_{f, \boldsymbol{\lambda}} \left\{ \Phi(f, \boldsymbol{\lambda}) := \frac{\gamma}{2} \|P_f - \mathcal{R}f - \psi_{D,\boldsymbol{\lambda}}\|_{L^2([0,2\pi] \times \mathbb{R})}^2 + \|\nabla f\|_{L^1(\Omega)} \right\}, \quad (2.20)$$

where $\psi_{D,\boldsymbol{\lambda}}$ is the function in the right side of (2.18), $\|\nabla f\|_{L^1(\Omega)}$ the TV-regularization term, and γ the regularization parameter. Before application of (2.20), we may determine D by the segmentation using simple thresholding [13].

In order to solve the problem (2.20), we use the augmented Lagrangian method [11, 27, 31]. By introducing auxiliary variable $\mathbf{q} = \nabla f$, we solve the following problem.

$$\min_{f, \boldsymbol{\lambda}, \mathbf{q}} \max_{\boldsymbol{\tau}} \int_{\Omega} |\mathbf{q}| dx + \frac{\gamma}{2} \int_0^{2\pi} \int_{\mathbb{R}} |P_f - \mathcal{R}f - \psi_{D,\boldsymbol{\lambda}}|^2 d\varphi ds + \int_{\Omega} \boldsymbol{\tau} \cdot (\mathbf{q} - \nabla f) dx + \frac{r}{2} \int_{\Omega} |\mathbf{q} - \nabla f|^2 dx. \quad (2.21)$$

The augmented Lagrangian algorithm is summarized in the Algorithm 2.1.

Algorithm 2.1.

1. Initialization: $\mathbf{q}_0 = \boldsymbol{\tau}_0 = \mathbf{0}$, $f^0 = 0$ and $\boldsymbol{\lambda}_0$ chosen by solving the problem (18) in [26].
2. For fixed multiplier $\boldsymbol{\tau}^k$, solve

$$\begin{aligned} (f^{k+1}, \boldsymbol{\lambda}^{k+1}) = \arg \min_{f, \boldsymbol{\lambda}} & \frac{\gamma}{2} \int_0^{2\pi} \int_{\mathbb{R}} |P_f - \mathcal{R}f - \psi_{D,\boldsymbol{\lambda}}|^2 d\varphi ds \\ & - \int_{\Omega} \boldsymbol{\tau}^k \cdot \nabla f dx + \frac{r}{2} \int_{\Omega} |\mathbf{q} - \nabla f|^2 dx \end{aligned} \quad (2.22)$$

and solve

$$\mathbf{q}^{k+1} = \arg \min_{\mathbf{q}} \int_{\Omega} |\mathbf{q}| dx + \int_{\Omega} \boldsymbol{\tau}^k \cdot \mathbf{q} dx + \frac{r}{2} \int_{\Omega} |\mathbf{q} - \nabla f|^2 dx \quad (2.23)$$

3. Update $\boldsymbol{\tau}^{k+1}$ by

$$\boldsymbol{\tau}^{k+1} = \boldsymbol{\tau}^k + r(\mathbf{q}^{k+1} - \nabla f^{k+1}) \quad (2.24)$$

We solve the problem (2.22) iteratively by

$$\begin{aligned} f^{k+1} = \arg \min_f & \frac{\gamma}{2} \int_0^{2\pi} \int_{\mathbb{R}} |P_f - \mathcal{R}f - \psi_{D,\boldsymbol{\lambda}^k}|^2 d\varphi ds - \int_{\Omega} \boldsymbol{\tau}^k \cdot \nabla f dx \\ & + \frac{r}{2} \int_{\Omega} |\mathbf{q} - \nabla f|^2 dx, \end{aligned} \quad (2.25)$$

$$\boldsymbol{\lambda}^{k+1} = \arg \min_{\boldsymbol{\lambda}} \|P_f - \mathcal{R}f^{k+1} - \psi_{D,\boldsymbol{\lambda}}\|_{L^2([0,2\pi] \times \mathbb{R})}^2. \quad (2.26)$$

The nonlinear problem (2.26) is solved by using the standard Newton's method as in [26].

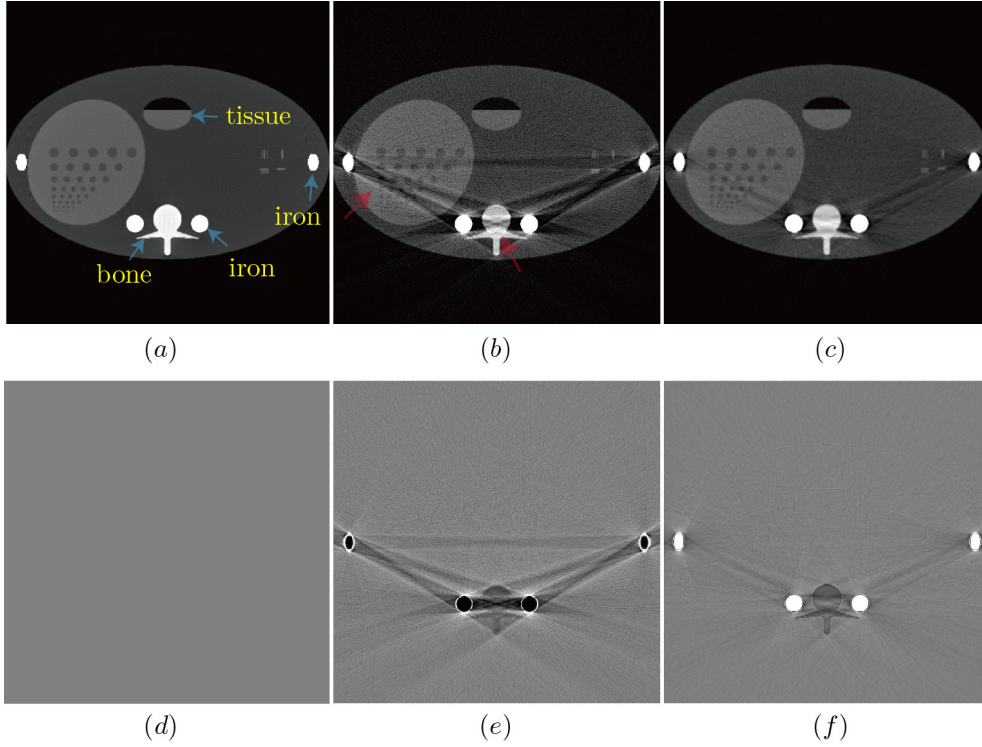


Fig. 2.3. Simulation result using the proposed method. (a). abdomen phantom containing for metallic objects (irons), (b). uncorrected CT image $\mathcal{B}[P_f]$, (c). corrected image obtained from (2.20) with the regularization parameter $\gamma = 20$. Figure (d)-(f) depict the difference image to the image (a) ($C=1750$ HU/ $W=6500$ HU for CT images (a)-(c), and $C=-1000$ HU/ $W=6000$ HU for difference images (d)-(e)).

3. Results

Numerical simulations were conducted to test the performance of the proposed method. For the numerical simulation, the projection data P_f described in (2.2) is generated for the tube voltage 80 kVp [12]. Poisson noise is added to the measured P_f with the 0.01 noise level (i.e. standard deviation of P_f on the outside of support of P_f). In our simulations, other effects such as photon scattering and photon starvation effect were not modeled. To simulate beam hardening artifacts, we superposed four iron objects in abdomen phantom as shown in Fig. 2.3 (a). In this numerical simulation, f is assumed as

$$f(\mathbf{x}, E) = f_0(\mathbf{x}, E) + \sum_{i=1}^4 \mu_{\text{iron}}(E) \chi_{D_i}(\mathbf{x}), \quad (3.1)$$

where $\mu_{\text{iron}}(E)$ is the linear attenuation coefficient of the iron given in Fig. 2.2 and f_0 is the background image consisting of bone and tissues. The uncorrected image in Fig. 2.3 (b) is obtained by the FBP algorithm in (2.4). The proposed method was applied to remove the severe streaking and shadow artifacts from the reconstructed image $\mathcal{B}[P_f]$. Here, the regularization parameter $\gamma = 20$ was empirically chosen to minimize the normalized root mean square difference (NRMSD) [17] between the corrected image (f_{cor}) and the metal artifacts-free image

$B[P_{f_0}]$ (See Fig. 2.3 (a)) on $\Omega \setminus D$; the NRMSD is given by

$$\text{NRMSD}(\%) = \left[\frac{\int_{\Omega \setminus D} |f_{\text{cor}}(\mathbf{x}) - B[P_{f_0}](\mathbf{x})|^2 d\mathbf{x}}{\int_{\Omega \setminus D} |B[P_{f_0}](\mathbf{x})|^2 d\mathbf{x}} \right]^{1/2} \times 100. \quad (3.2)$$

Fig. 2.3 (c) shows that streaking and shadow artifacts are substantially reduced in the corrected image. Moreover, morphological structure of phantom corrupted by metal artifacts are considerably recovered. With the aid of the regularization term in (2.20), the proposed algorithm suppresses the streaking artifacts due to noise as well. The remaining metal artifacts in Fig. 2.3 (c) may be mainly due to our model assumption error in (2.15).

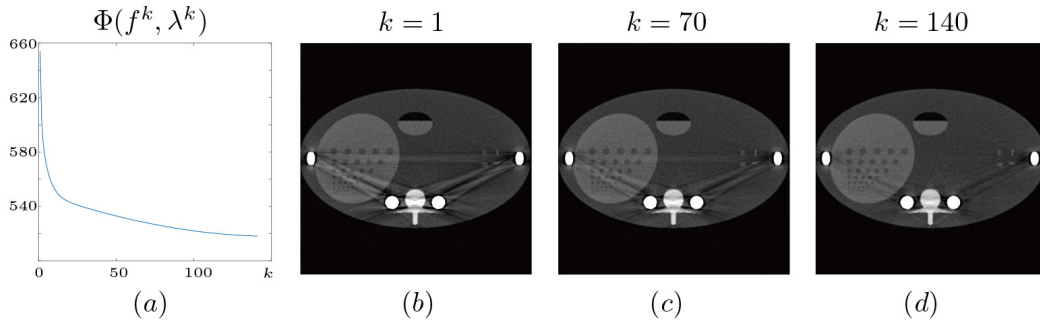


Fig. 3.1. Figure (a) depicts the convergence curve which shows the energy functional $\Phi(f^k, \lambda^k)$ in (2.20) as a function of iteration k . Figures (b)–(d) show the reconstructed image f^k for $k = 1, 70, 140$, respectively.

Fig. 3.1 (a) depicts the convergence curve which shows the energy functional $\Phi(f^k, \lambda^k)$ in (2.20) as a function of iteration k . Fig. 3.1 (b)–(d) illustrate the reconstructed image f^k for $k = 1, 70, 140$, respectively. Fig. 3.1 shows that the sequence $\{\Phi(f^k, \lambda^k)\}$ converges for the initial parameter $(0, \lambda^0)$, where λ^0 is chosen by solving the problem (18) in [26]. Streaking and shading artifacts in f^k are reduced for the number of iteration increasing. (See Fig. 3.1 (b)–(d))

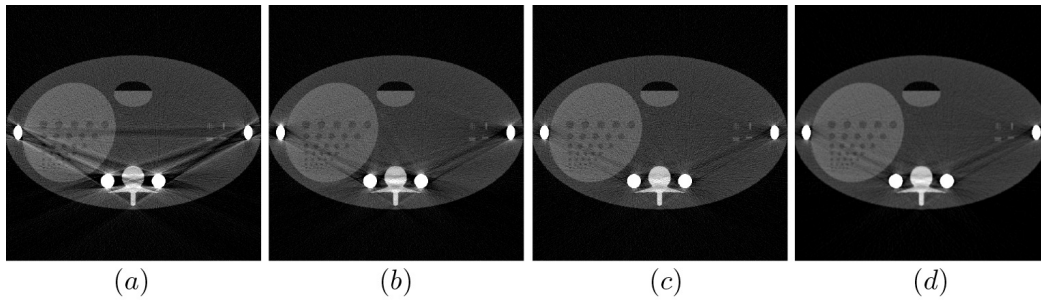


Fig. 3.2. Comparison between the proposed method and other existing methods. (a). uncorrected CT image (b). empirical beam hardening correction (EBHC) method [14] (c). metal artifact correction method (MAC-BC) [26]. (d). the proposed method with parameter $\gamma = 20$. ($C=1750$ HU/ $W=6500$ HU for all CT images).

Fig. 3.2 shows the comparison between the proposed method with other existing methods such as the empirical beam hardening correction (EBHC) methods [14] and the metal artifact correction method (MAC-BC) proposed in [26]. Compared with EBHC and MAC-BC methods,

the proposed method effectively reduces the streaking artifacts caused by metals and noise without generating new streaking artifacts. For the quantitative evaluation of the algorithms performance, NRMSD (%) was computed on $\Omega \setminus D$. The NRMSD of uncorrected, EBHC, MAC-BC and proposed method were 36.34, 29.24, 28.22 and 15.56, respectively. In terms of NRMSD, the proposed method shows better performance than those two methods.

4. Discussion and Conclusion

The metal artifact reduction in CT has been an important and challenging issue for dental and medical fields, as MAR is more demanding for various applications including the forensic dental identification and the rapid prototyping of dental structures.

We knew that the beam hardening causes the discrepancy between the projection data (P) and its orthogonal projection (ΠP) onto the range space of the Radon transform. Although the least square-based algorithm is to find an image f which minimizes the fidelity term $\|P - \mathcal{R}f\|$, its fundamental nature uses the orthogonal projection ΠP instead of P , regardless of size of the discrepancy $\Pi P - P$. Hence, with this least square approach, streaking and shadow artifacts due to the beam hardening may be unavoidable. We observe that the streaking and shadow artifacts are closely linked to the size of the discrepancy $\Pi P - P$. From Fig. 2.1, the inconstancy of P occurs in a small local region, whereas the error $\Pi P - P$ appears globally. Hence, it seems to be desirable to amend P in the small local region to be consistent in the sinogram space, because P is somehow consistent in most regions.

Recently, Park *et al* [26] has derived the analytic form of a beam hardening corrector, which aims to express the inconsistency of P in terms of the geometries of metallic objects. Hence, given prior knowledge of metal geometries, it is possible for this corrector to be used to handle the local inconsistency of P . Taking advantage of this beam-hardening corrector, a minimization model is proposed to provide beam hardening-free images. The proposed method with an optimal regularization parameter effectively reduce the streaking artifacts in reconstructed image as well as noise artifacts. The proposed model is mainly based on the (2.17), which does not consider the photon starvation effect [3]. Further research is necessary to deal with the streaking artifacts caused by the photons starvation.

Acknowledgements. This work was supported by Samsung Science & Technology Foundation (No. SSTF-BA1402-01).

References

- [1] M. Abdoli, M. R. Ay, A. Ahmadian, R. A. Dierckx and H. Zaidi, Reduction of dental filling metallic artifacts in CT-based attenuation correction of PET data using weighted virtual sinograms optimized by a genetic algorithm, *Medical Physics*, **37** (2010), 6166–6177.
- [2] R. E. Alvarez and A. Macovski. Energy-selective reconstructions in X-ray computerized tomography. *Physics in Medicine and Biology*, **21** (1976), 733–744.
- [3] Barrett, J. F.; Keat, N. Artifacts in CT: recognition and avoidance1, *Radiographics* **24** (2004), 1679–1691.
- [4] M. Bazalova, L. Beaulieu, S. Palefsky and F. Verhaegen, Correction of CT artifacts and its influence on monte carlo dose calculations, *Medical Physics*, **34** (2007), 2119–2132.
- [5] F. E. Boas and D. Fleischmann, CT artifacts: causes and reduction techniques. *Imaging in Medicine*, **4** (2012), 229–240.

- [6] R.N. Bracewell and A.C. Riddle, Inversion of fan-beam scans in radio astronomy, *The Astrophysical Journal*, **150** (1967), 427.
- [7] J. Bushberg, J. Seibert, E. Leidholdt Jr, and J. Boone, The essential physics of medical imaging, Lippincott Williams & Wilkins, 2002.
- [8] E. Van, D. Castele, D. V. Dyck, J. Sijbers, E. Raman, A model-based correction method for beam-hardening artefacts in X-ray microtomography, *Journal of X-ray Science and Technology*, **12** (2004), 43–57.
- [9] B. De Man, J. Nuyts, P. Dupont, G. Marchal, and P. Suetens, An iterative maximum-likelihood polychromatic algorithm for CT, *IEEE Transactions on Medical Imaging*, **20** (2001), 999–1008.
- [10] I. A. Elbakri and J. A. Fessler, Statistical image reconstruction for polyenergetic X-ray computed tomography, *IEEE Transactions on Medical Imaging*, **21** (2002), 89–99.
- [11] M. R. Hestenes, Multiplier and gradient methods, *Journal of Optimization Theory and Applications*, **4** (1969), 303–320.
- [12] J. H. Hubbell and S. M. Seltzer, Tables of X-ray mass attenuation coefficients and mass energy-absorption coefficients, *National Institute of Standards and Technology*, 1996.
- [13] W. A. Kalender, R. Hebel and J. Ebersberger, Reduction of CT artifacts caused by metallic implants, *Radiology*, **164** (1987), 576–577.
- [14] Y. Kyriakou, E. Meyer, D. Prell, and M. Kachelrieß, Empirical beam hardening correction (EBHC) for CT, *Medical Physics*, **37** (2010), 5179–5187.
- [15] R. M. Lewitt and R. H. T. Bates, Image reconstruction from projections: Iv: Projection completion methods (computational examples), *Optik*, **50** (1978), 269–278.
- [16] C. Lemmens, D. Faul, and J. Nuyts, Suppression of metal artifacts in CT using a reconstruction procedure that combines MAP and projection completion, *IEEE Transactions on Medical Imaging*, **28** (2009), 250–260.
- [17] A. Mehranian, M. R. Ay, A. Rahmim and H. Zaidi, X-ray CT metal artifact reduction using wavelet domain sparse regularization, *IEEE Transactions on Medical Imaging*, **32** (2013), 1707–1722.
- [18] N. Menvielle, Y. Goussard, D. Orban, and G. Soulez, Reduction of beam-hardening artifacts in X-ray CT, *Engineering in Medicine and Biology Society, 27th Annual International Conference of the, IEEE 2005*, 1865–1868.
- [19] E. Meyer, R. Raupach, M. Lell, B. Schmidt and M. Kachelrieß, Normalized metal artifact reduction (NMAR) in computed tomography, *Medical Physics*, **37** (2010), 5482–5493.
- [20] J. Müller and T. M. Buzug, Spurious structures created by interpolation-based CT metal artifact reduction, *Proc. SPIE 7258, Medical Imaging 2009*, 1Y1–1Y8.
- [21] F. Natterer, The mathematics of computerized tomography, Springer, 1986.
- [22] J. A. O’Sullivan and J. Benac, Alternating minimization algorithms for transmission tomography, *IEEE Transactions on Medical Imaging*, **26** (2007), 283–297.
- [23] H. S. Park, J. K. Choi, K. R. Park, K. S. Kim, S. H. Lee, J. C. Ye and J. K. Seo, Metal artifact reduction in CT by identifying missing data hidden in metals, *Journal of X-ray Science and Technology*, **21** (2013), 357–372.
- [24] H. S. Park, J. K. Choi and J. K. Seo, Characterization of metal artifacts in X-ray computed tomography, *arXiv preprint arXiv:1406.0318*, 2014.
- [25] H. S. Park, Y. E. Chung and J. K. Seo, Computed tomographic beam hardening artefacts: mathematical characterization and analysis, *Philosophical Transactions of the Royal Society A*, **373** (2015), 20140388.
- [26] H. S. Park, D. Hwang and J. K. Seo, Metal artifact reduction for polychromatic X-ray CT based on a beam hardening corrector, *IEEE Transactions on Medical Imaging*, **35** (2016), 480–487.
- [27] R. T. Rockafellar, A dual approach to solving nonlinear programming problems by unconstrained optimization, *Mathematical Programming*, **5** (1973), 354–373.
- [28] J. C. Roeske, C. Lund, C. A. Pelizzari, X. Pan and A.J. Mundt, Reduction of computed tomogra-

- phy metal artifacts due to the fletcher-suit applicator in gynecology patients receiving intracavitary brachytherapy, *Brachytherapy*, **2** (2003), 207–214.
- [29] L. Rudin, S. Osher and E. Fatemi, Nonlinear total variation based noise removal algorithms, *Physica D: Nonlinear Phenomena*, **60** (1992), 259–268.
- [30] S. Schüller, S. Sawall, K. Stannigel, M. Hülsbusch, J. Ulrici, E. Hell and M. Kachelrieß, Segmentation-free empirical beam hardening correction for CT, *Medical Physics*, **42** (2015), 794–803.
- [31] X. Tai and C. Wu, Augmented Lagrangian method, dual methods and split Bregman iteration for ROF model, *Scale space and variational methods in computer vision*, **5567** (2009), 502–513.
- [32] G. Wang, D. L. Snyder, D. A. O’Sullivan, M. W. Vannier. Iterative deblurring for ct metal artifact reduction. *IEEE Transactions on Medical Imaging*, **15** (1996), 657–664.